International Scientific Conference 20 UNITECH 26

INTERNATIONAL SCIENTIFIC CONFERENCE
19-21 November 2026
GABROVO

OPTICAL ABSORBTION IN THE SINGLE-STEP SPHERICAL QUANTUM DOT

S. E. Okan[1,*], F. K. Boz[1], A. Bilekkaya[2], S. Aktas[1]

[1]*Trakya University, Physics Department, Edirne, Turkey*
[2]*Trakya University, Vocational School of Technical Science, Edirne, Turkey*
**Corresponding author: erolokan@trakya.edu.tr*

Abstract

The employment of quantum dots in optoelectronic devices motivated this theoretical study of single-step potential $GaAs/Al_xGa_{1-x}As/AlAs$ spherical quantum dot. The electron's energy states and electronic wave functions were calculated using the Runge-Kutta numerical method within the effective mass approach. The presence of a donor impurity atom in the device was also considered. Having the energy states and wave functions, the total absorption coefficients of $1s-1p, 1p-1d, 1p-2s, 2s-2p, 2p-2d$ transitions was obtained. It was determined how reducing the $Al_xGa_{1-x}As$ layer thickness, which creates the barrier potential, while increasing the $GaAs$ core radius in the single-step spherical quantum dot, causes variations in the electronic and optical properties. The inclusion of an impurity in the structure shifts the total absorption coefficients to higher or lower photon energies depending on the wave function localization. The results obtained can help to regulate energy spectra in newly designed optoelectronic devices.

Keywords: Quantum Dot, Impurity, Energy State, Absorption Coefficients

INTRODUCTION

The use of quantum dots (QD) in nanotechnological devices has brought an increasing scientific interest to research on such low-dimensional structures. In the last two decades, semiconductor QDs have been used in solar panels [1,2], optoelectronic devices [3,4], and bioimaging in medicine [5] depending on their optical properties. QDs are favorable light sources for visible photonics. The Ni^{2+} ion doped QDs in perovskite class in supersaturated recrystallization synthetic approach and they were shown to be the photodiodes emitting bright blue light [6]. Another series of blue, red, and green light-emitting QD diodes obtained by spin coating were reported to work in high performance [7]. High efficiency in working conditions has been achieved for CdSe/CdS quantum dots [8,9].

On the theoretical side, it has been shown that the energy states of multilayer quantum dots can be controlled by their geometrical constitution parameters and materials the dots are made of. The geometrical parameters of semiconductor components of various multilayered QDs [10-12] and the position of impurity in these devices [13-15] have been proven to be effective on the energy states. Beyond, the linear and nonlinear absorption coefficients in quantum wells, quantum well wires, and QD structures have theoretically been investigated to determine their optoelectronic properties. These low dimensional structures' electronic and optical properties are calculated under external electric, external magnetic, and (or) laser fields which all probe the device. Nevertheless, the external fields reshape the profile of the electron confining potential and thus change the subband energies as well as the electronic wave functions. In turn, the linear and nonlinear optical coefficients of heterostructures such as optical absorption coefficients (OACs) and refractive indexes

This is an open access article licensed under Creative Commons Attribution 4.0 International
Print ISSN: 1313-230X, Online ISSN: 3033-1404

(RIs) are greatly affected [16-27]. Specifically, how the Al concentration in the electron confining region affects the optical properties of the structure with and without impurity atoms has been shown in $Al_xGa_{1-x}As/Al_{0.3}Ga_{0.7}As/Al_yGa_{1-y}As/Al_{0.3}Ga_{0.7}As$ QDs which are in general described as multilayer spherical quantum dots (MSQD) [22]. Changes in transition energies, oscillation intensities, and absorption coefficients have been observed in parabolic MSQDs that can be grown by varying the layer thicknesses compared to other different forms [23]. Also, the effects of core radius, layer thickness, and externally applied electric and magnetic field on third harmonic generation (THG) in parabolic MSQDs with and without impurity atoms were studied. In the results, they showed that the amplitude of THG tends to increase or decrease depending on the aforementioned variables, increasing the applied electric field intensity causes the maximum of the THG amplitude to be red-shifted, but increasing the applied magnetic field strength causes a blue shift [24].

In an experimental study, core/shell-1/shell-2 quantum dots were manufactured and they were shown to increase quantum fluorescence efficiency compared to those of other core/shell structures [28]. Such experimental studies naturally encourage theoretical research on these structures. The blueshifts were calculated in the intersubband optical properties of electrons in $InGaN/GaN$ spherical core-shell quantum dots under the built-in electric field [29]. In a study where the intra-miniband absorption coefficients for the transitions between the 1s and 1p electronic states in the $GaAs/Al_xGa_{1-x}As$ core/shell spherical quantum dot show red and blue shifts depending on the core and shell size [30]. Also, the optical properties of hydrogenic impurity in the inhomogeneous infinite spherical quantum dot are strongly dependent on the inner radius and thickness of the shell [31]. In addition, the absorption coefficients of $1s \rightarrow 2p$ and $1p \rightarrow 1d$ transitions were calculated depending on the dimensions of the core/shell/shell quantum dot, the position of a donor atom it contains, and the externally applied magnetic field. It has been shown that the amplitudes of the linear, non-linear, and total optical absorption coefficients depend on the core/shell dimensions [32].

A single stepped $GaAs/Al_xGa_{1-x}As/AlAs$ spherical quantum dot is considered. Depending on the geometric parameters of the QD, the energy states with and without the donor atom are calculated. The appropriate transition energies between these states are found, and the behavior of the linear and non-linear absorption numbers in total is investigated in this work.

THEORY

The single step $GaAs/Al_xGa_{1-x}As/AlAs$ spherical quantum dot structure, in which the $GaAs$ sphere enveloped by the $Al_xGa_{1-x}As$ spherical shell for different aluminum concentrations, is considered. These are then assumed to be enveloped by the infinite potential of an $AlAs$ shell. The cross-sectional view and potential energy profile of the quantum dot are schematically shown in Figs. 1a and b, respectively.

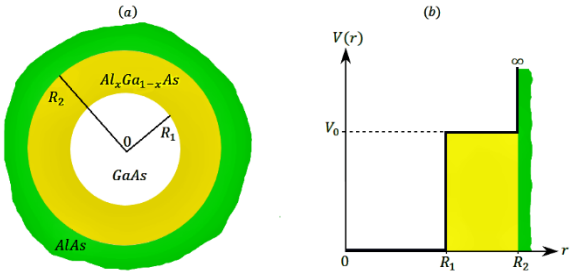


Fig. 1. (**a**) *Cross-sectional view of spherical multilayered quantum dot together with its semiconductor composition.* (**b**) *The corresponding one-step potential energy profile of the quantum dot is sketched in Fig.1a.*

The Hamiltonian of an electron in the QD with a hydrogenic impurity placed in the center of the structure can be written

$$H = H_0 + bU(r) \qquad (1)$$

where $U(r)$ represents the electron–impurity interaction in a dielectrically non-uniform

system. The constant b in Eq. (1) is unity if the impurity exists, and is zero if the impurity is absent. The potential energy $U(r)$ of interaction potential between the electron and the on-center impurity ion is the solution of the Poisson equation given in the form of.

$$U(r) = \begin{cases} -\frac{e^2}{\varepsilon_1 r} + \frac{e^2}{\varepsilon_1 R_1}\left(1-\frac{\varepsilon_1}{\varepsilon_2}\right) + \frac{e^2}{\varepsilon_2 R_2}\left(1-\frac{\varepsilon_2}{\varepsilon_3}\right), & r \le R_1 \\ -\frac{e^2}{\varepsilon_2 r} + \frac{e^2}{\varepsilon_2 R_2}\left(1-\frac{\varepsilon_2}{\varepsilon_3}\right), & R_1 < r \le R_2 \\ -\frac{e^2}{\varepsilon_3 r}, & r \ge R_2 \end{cases} \quad (2)$$

where ε_1, ε_2, and ε_3 in Eq.2 are the dielectric constants of the $GaAs$, $Al_xGa_{1-x}As$ and $AlAs$, respectively [10,11,33]. If the electron experiences only the confining potential of QD, its Hamiltonian, H_0 in Eq.1 is

$$H_0 = -\frac{\hbar^2}{2}\vec{\nabla}.\left[\frac{1}{\mu(r)}\vec{\nabla}\right] + V(r) \quad (3)$$

where $\mu(r)$ is the effective mass of the electron with the constant masses μ_1 and μ_2 expressed as

$$\mu(r) = \begin{cases} \mu_1 & r \le R_1 \\ \mu_2 & R_1 < r \le R_2 \end{cases}. \quad (4)$$

The spherically symmetric potential depending on position is

$$V(r) = \begin{cases} 0 & r \le R_1 \\ V_0 & R_1 < r \le R_2 \\ \infty & r \ge R_2 \end{cases}, \quad (5)$$

where V_0 is the height of the barrier potential. and R_2 in Eq.5 are the GaAs core radius and the outer radius of $Al_xGa_{1-x}As$ layer, respectively. Therefore, $R_B = R_2 - R_1$ is the thickness of the spherical shell.

Since the confining potential depends on the radius of the spherically symmetric QD Schrödinger equation as well in spherical coordinates is given by

$$-\frac{\hbar^2}{2}\vec{\nabla}.\left[\frac{1}{\mu(r)}\vec{\nabla}\psi_{nlm}\right] + [V(r) + bU(r)]\psi_{nlm} = E_{nl}\psi_{nlm} \quad (6)$$

where the ansatz is given by $\psi_{nlm}(r,\theta,\varphi) = R_{nl}(r)Y_{lm}(\theta,\varphi)$ as $R_{nl}(r)$ and $Y_{lm}(\theta,\varphi)$ being the radial wave function and the spherical harmonics. The dipole transitions of an electron in the inter-subband are calculated by applying the $\Delta l = \pm 1$ selection rule, in the study. This corresponds to the transitions for the principal quantum numbers $n = 1, 2,$ and the angular momentum quantum numbers $l = 0(s), 1(p), \text{and } 2(d)$ with the magnetic quantum number $m = 0$ are considered. Considering the effective Bohr radius $a^* = \varepsilon_1\hbar^2/\mu_1 e^2$ and the Rydberg energy $R^* = \mu_1 e^4/2\hbar^2\varepsilon_1^2$ as the reduced units, the Schrödinger equation is reduced to the radial form of

$$[-\frac{\mu_1}{\mu(r)}\frac{d^2}{dr^2} - \frac{\mu_1}{\mu(r)}\frac{2}{r}\frac{d}{dr} + \frac{l(l+1)}{r^2} + bU(r) + V(r)]R_{nl} = E_{nl}R_{nl}. \quad (7)$$

The energy levels and wavefunctions can be found in the solution of Eq. (7) by using the fourth-order Runge-Kutta method with and without an on-center impurity atom. As well know, the solution procedure of this method is controlled by the specified error accuracy at each step of the integration. The details of the Runge-Kutta method can be found in our previous works [11,12, 33,34].

Since the wave functions and energies of the states are calculated, we can examine the optical properties of the system by calculating the possible transitions between the states. The total absorption coefficient is written as

$$\alpha(\omega, I) = \alpha^1(\omega) + \alpha^3(\omega, I) \quad (8)$$

where the terms $\alpha^1(\omega)$ and $\alpha^3(\omega, I)$ are denoted the linear and third-order nonlinear optical absorption coefficients, respectively[19, 25, 35]. The optical absorption coefficients in Eq. 8 are given by $\alpha^1(\omega)$

$$= \hbar\omega\sqrt{\frac{\mu}{n_r^2\epsilon_0}}\left[\frac{\sigma\left|M_{if}\right|^2\tau_{if}^{-1}}{\left(E_{if}-\hbar\omega\right)^2 + \hbar^2\tau_{if}^{-2}}\right] \quad (9)$$

and

$$\alpha^3(\omega, I) = -\hbar\omega \sqrt{\frac{\mu}{n_r^2 \epsilon_0}} \left(\frac{2I}{n_r \epsilon_0 c}\right) x$$

$$\frac{\sigma |M_{if}|^4 \tau_{if}^{-1}}{\left[\left(E_{if} - \hbar\omega\right)^2 + \hbar^2 \tau_{if}^{-2}\right]^2} \quad (10)$$

$$x\left\{1 - \frac{|M_{ff} - M_{ii}|^2}{4|M_{if}|^2} \frac{\left[3E_{if}^2 - 4E_{if}\hbar\omega + (\hbar\omega)^2 - \tau_{if}^{-2}\right]}{E_{if}^2 + \hbar^2 \tau_{if}^{-2}}\right\}$$

where I is the incident optical intensity, τ_{if} is the relaxation time for states f and i, n_r is the refractive index, σ is the electron density. The transition energy E_{if} is the energy difference between the final and initial states. The dipole transition matrix elements M_{if} in Eqs 9 and 10 is expressed as

$$M_{if} = \left| e \int_0^{2\pi} \int_0^{\pi} \int_0^{\infty} \psi_f \, r \cos\theta \, \psi_i \, r^2 \, dr \sin\theta \, d\theta \, d\varphi \right| \quad (11)$$

where assumed that the electromagnetic radiation is polarized throughout the z-axis.

RESULTS AND DISCUSSIONS

In the $GaAs$ core, the effective mass of the electron and the permittivity were taken to be $\mu_1 = 0.067 m_e$, where m_e being the free electron mass, and $\varepsilon_1 = 13.18$, respectively. These parameters calculated from $\mu_2 = (0.067 + 0.083x)m_e$ and $\varepsilon_2 = 13.18 - 3.12x$ for the $Al_xGa_{1-x}As$ shell while the permittivity of outer shell $AlAs$ was $\varepsilon_3 = 10.06$. The alloy concentration chosen was $x = 0.30474$. The barrier potential energy was $V_0 = 228\, meV$ [11]. The effective Bohr radius and the effective Rydberg energy are thus found as $a^* \cong 104.48$ Å and $R^* \cong 5.25\, meV$, respectively. The impurity was supposed to be located at the center of the QD in all calculations. The single electron eigenenergies for $l = 0(s)$, $l = 1(p)$, and $l = 2(d)$ states and both cases with and without an impurity atom. The number 1 in front of s, p and d was shown if it was the first-order (the lowest energy) solution as the number 2 in front of the concerning letters symbolizes the second-order solutions.

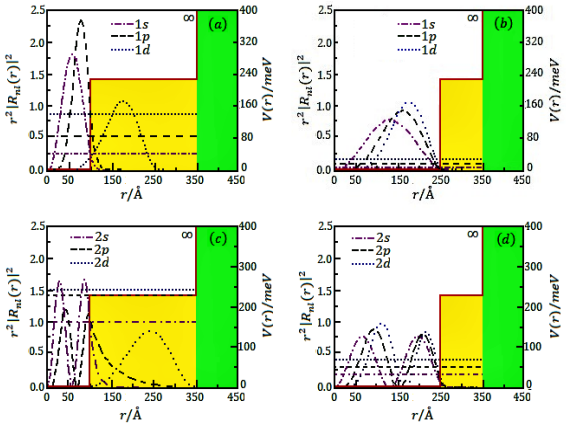


***Fig. 2**. Radial probability distribution of electron and its energy states in the spherical $GaAs/Al_xGa_{1-x}As/AlAs$ quantum dot containing a center donor impurity, (**a**) $1s$, $1p$ and $1d$ transitions for $R_1 = 100$ Å and $R_B = 250$ Å, (**b**) same as in Fig. 2a, but for $R_1 = 250$ Å and $R_B = 100$ Å, (**c**) same as in Fig. 2a, but for $2s$, $2p$ and $2d$ transitions, (**d**) same as in Fig. 2a, but for $R_1 = 250$ Å and $R_B = 100$ Å.*

The radial probability distributions and energy levels for two different values of R_1 and R_B $(= R_2 - R_1)$ couple when the impurity is in the center of the QD are shown for $1s$, $1p$ and $1d$ levels in Figs. $2a$ and $2b$ in which $R_1 = 100$ Å and $R_1 = 250$ Å, respectively. Figs. $2c$ and $2d$ are respectively the same as in Figs. $2a$ and $2b$ but for $2s$, $2p$, and $2d$ levels. With the $R_1 = 100$ Å, the probability distributions of the $1s$,$1p$, and $2s$ probabilities are localized in the $GaAs$ region. The probability noticeably overflows into the $Al_xGa_{1-x}As$ barrier region for the $2p$ state while the electron leaks into $Al_xGa_{1-x}As$ region when it is in $1d$ or $2d$ states. When the R_1 value increases and the R_B value decreases, it is seen that the probability distributions for all energy states are in the $GaAs$ region as seen in Figs. $2b$ and $2d$. The differences between all energies decrease with the radius $R_1 = 250$ Å.

Let us define the allowed transition energies depending on R_1 expansion without and with the impurity by E_{if}^0 and E_{if}^1 in Figs. $3a$-$3e$, respectively. While $E_{if}^0 < E_{if}^1$ for

$1s-1p$ transitions, these two energies are almost equalized in $1p-1d$ transitions.

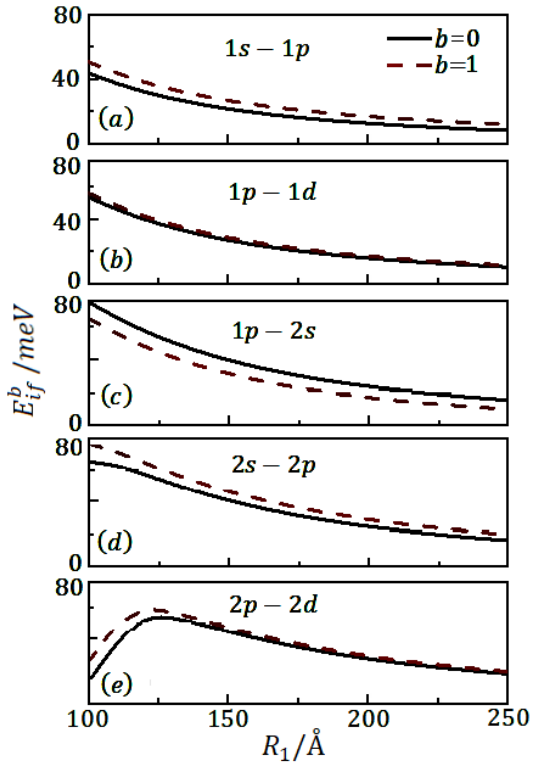


Fig. 3. *Variations of the transition energies as a function of the R_1 in the spherical $GaAs/Al_xGa_{1-x}As/AlAs$ quantum dot (**a**) for $1s-1p$, (**b**) for $1p-1d$, (**c**) for $1p-2s$, (**d**) for $2s-2d$, and (**e**) for $2p-2d$. Full lines are for no-impurity cases and dashed (red) lines are for a center-impurity existing case.*

When compared to $1s-1p$ transitions, the situation is reversed in $1p-2s$ transitions as $E_{if}^{0} > E_{if}^{1}$ is observed. The energies of these three transitions are characteristically similar to the variation of the binding energy of an electron in an infinite quantum well depending on the well width. In the $2s-2p$ and $2p-2d$ transitions, the race between states with and without the impurity turns in favor of E_{if}^{1} with $E_{if}^{0} < E_{if}^{1}$. On the other hand, both transition energy characteristics, slightly with the $2s-2p$ and very distinctly with the $2p-2d$, are similar to the variation of the binding energies depending on the well width in finite quantum wells. Especially in the $2p-2d$ transition, the energy starts to increase from $R_1 = 100$ Å and reaches its maximum value around $R_1 = 125$ Å. After this point, the energies decrease smoothly with decreasing barrier thickness in R_1 expansions.

The total absorption coefficients depending on the photon energy $E_{ph} = \hbar\omega$ for the $1s-1p$, $1p-1d$, $1p-2s$, $2s-2p$, $2p-2d$ transitions are shown for $R_1 = 100$ Å in Fig. $4a$ and for $R_1 = 200$ Å in Fig.$4b$. The calculations were again performed for the impurity-free and impurity-containing cases as earlier. In all transitions, except the $2p-2d$ transition, the total absorption coefficient peak values shifted towards smaller photon energies while the $GaAs$ radius increased. In the $2p-2d$ transition, $2d$ energy level is above the step potential for $R_1 = 100$ Å while it is smaller than the step potential for $R_1 = 200$ Å. This behavior has also been observed in relevant studies. It is pointed out in the literature that the electronic probability distribution is localized into the barrier for narrow wells [10, 35]. Fig. $2c$ is a good example of this behavior. This behavior of the probability distributions strongly affects the dipole transition matrix element used in the calculation of the absorption coefficients. Because, as seen in Eq.11, M_{if} is calculated by using the initial and the final wave functions. In other words, at the narrow GaAs potential, the $2p$ and $2d$ wave functions are far away from each other compared to the wave functions at other energy levels.

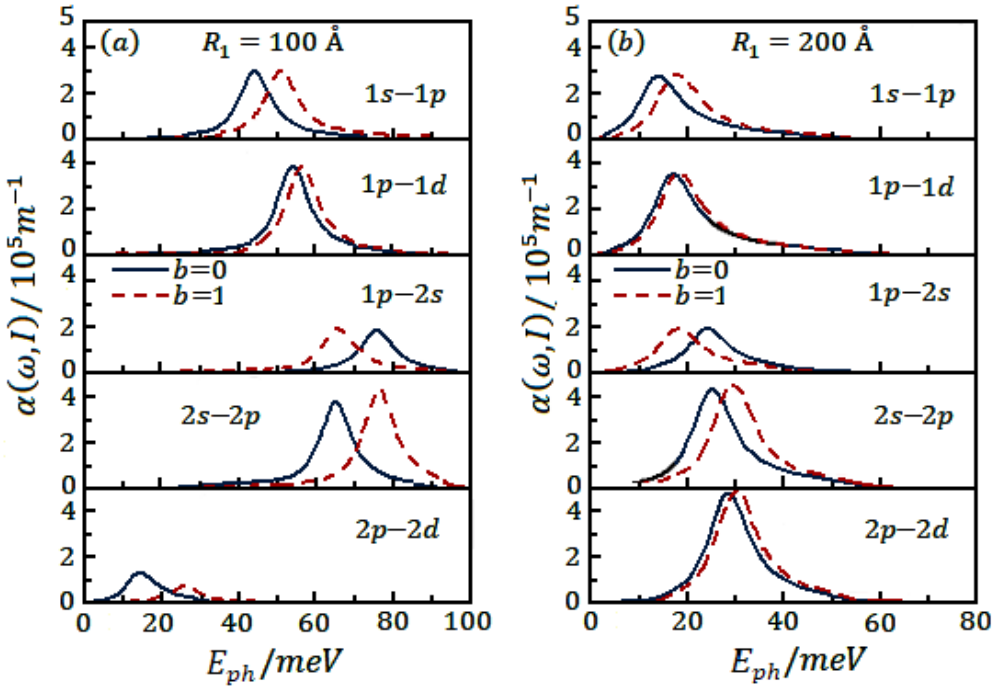


Fig. 4. *(**a**) The total absorption coefficients of a spherical $GaAs/Al_xGa_{1-x}As/AlAs$ quantum dot with and without impurity versus the photon energy for $R_1 = 100$ Å, (**b**) Same as in Fig. 4a, but for $R_1 = 200$ Å.*

In Figs 4a and 4b, the maximum peak values in the 1s-1p, 1p-1d, 2s-2p, and 2p-2d transitions of the total absorption coefficients with the impurity (b=1) have shifted to slightly larger photon energies compared to the same transitions without the impurity (b=0). For an explanation, we can consider the 1s-1p transition energies for b=0 and b=1 given in Fig. 3a. Accordingly, the transition energy of the b=1 is greater than that of the b=0. The same behavior is also observed for 1p-1d, 2s-2p, and 2p-2d transitions. The 1p-2s transitions in Fig. 3c differ from the other transitions. It is seen that the b=1 transition energies are smaller than those of the b=0. Depending on this behavior, the peak value of the absorption coefficient in the case with the impurity atom occurs at lower photon energy than the peak value of the absorption coefficient in the case without the impurity atom as seen in Figs 4a and 4b.

CONCLUSION

Best to our knowledge, the spherical $GaAs/Al_xGa_{1-x}As/AlAs$ quantum dot is studied first time, although the photon energies are not in the visible light spectrum.

REFERENCES

[1] Muthalif MPA, Sunesh ., and Choe Y. Enhanced light absorption and charge recombination control in quantum dot sensitized solar cells using tin doped cadmium sulfide quantum dots. Journal of Colloid and Interface Science 2019; 534:291-300.

[2] Jun HK, Careem MA, Arof AK. Quantum dot-sensitized solar cells— perspective and recent developments. A review of Cd chalcogenide quantum dots as sensitizers. Renewable and Sustainable Energy Reviews 2013;22:148-167.

[3] Bhattacharya P, Ghosh S. Stiff-Roberts AD. Quantum dot optoelectronic devices. Annual Review of Materials Research 2004;34:1-40.

[4] Park SH, Ahn D. Non-Polar Wurtzite $(11\bar{2}0)$ GaN/AlN Quantum Dots for Highly Efficient Opto-Electronic Devices. Electronics 2020; 9(8):1256.

[5] Kairdolf BA, Smith AM, Stokes TH, Wang MD, Young AN, Nie S. Semiconductor Quantum Dots for Bioimaging and Biodiagnostic Applications. Annual Review of Analytic Chemistry 2013;6:143–162.

[6] Pan GC, Bai X, Xu W, Chen X, Zhai Y, Zhu JY, Shao H, Ding N, Xu L, Dong B, Mao YL, Song H. Bright blue light emission of Ni^{2+} ion-doped $CsPbCl_x\ Br_{3-x}$ Perovskite quantum dots enabling efficient light-emitting devices. ACS Appl. Mater. Interfaces 2020;12(12):14195–14202.
[7] Yang Y, Zheng Y, Cao W, Titov A, Hyvonen J, Manders JR, Xue P, Holloway PH, Qian L. High-efficiency light-emitting devices based on quantum dots with tailored nanostructures. Nature Photonics 2015;9:259-265.
[8] Liu D, Liu J, Liu J, Liu S, Wang C, Ge Z, Hao X, Du N, Xiao H. The photovoltaic performance of CdS/CdSe quantum dots co-sensitized solar cells based on zinc titanium mixed metal oxides. Physica E 2020;115:113669.
[9] Elsinger L, Petit R, Acker FV, Zawacka NK, Tanghe I, Neyts K, Detavernier C, Geiregat P, Hens Z, Thourhout DV. Waveguide-Coupled Colloidal Quantum Dot Light Emitting Diodes and Detectors on a Silicon Nitride Platform. Laser Photonics Rev. 2021;15:2000230.
[10] Rabanian A, Neghabi M, Zadsar M, Jafari M. Theoretical studies of energy states of CdSe/ZnS/CdSe and ZnS/CdSe/ZnS quantum dots with an impurity. Material Science and Engineering B-Advanced Functional Solid-State Material 2021; 274:115489.
[11] Boz FK, Nisanci B, Aktas S, Okan SE. Energy levels of $GaAs/Al_xGa_{1-x}As/AlAs$ spherical quantum dot with an impurity. Applied Surface Science 2016;387:76-81.
[12] Boz FK, Aktas S, Bilekkaya A, Okan SE. Geometric effects on energy states of a hydrogenic impurity in a multilayered spherical quantum dot. Applied Surface Science 2009;255:6561-6564.
[13] Fakkahi A, Sali A, Jaouane M, Arraoui R. Hydrostatic pressure, temperature, and electric field effects on the hydrogenic impurity binding energy in a multilayered spherical quantum dot. Applied Physics A-Materials Science & Processing 2021;127:908.
[14] Mese AI, Cicek E, Ozkapi SG, Ozkapi B, Erdogan I. Calculation of Intradonor Normalized Transition Energy in Spherical Quantum Dots Made of Different Materials. Physica Status Solidi B-Basic Solid State Physics 2023:2300133.
[15] Mese AI, Cicek E, Erdogan I, Akankan O, Akbas H. The effect of dielectric constant on binding energy and impurity self-polarization in a $GaAs - Ga_{1-x}Al_xAs$ spherical quantum dot. Indian Journal of Physics 2017;91:263-268.
[16] Yesilgul U, Ungan F, Al EB, Kasapoglu E, Sari H, Sokmen I. Effects of the magnetic field, hydrostatic pressure and temperature on the nonlinear optical properties in symmetric double semi-V-shaped quantum well. Optical and Quantum Electronics 2016;48:560.
[17] Al EB, Peter AJ, Mora-Ramos ME, Ungan F. Theoretical investigation of nonlinear optical properties of Mathieu quantum well. European Physical Journal Plus 2023;138:49.
[18] Redouane E, El Ghazib H, Belaid W, Abboudid H, Jaboutie F, Joriof A, Zorkani I. The Confinement Profile Effect on the Optical Properties in Different Inverse-shaped Single $InGaN/GaN$ Quantum Wells. Iraqi Journal of Physics 2022;20:1-13.
[19] Bekar B, Boz FK, Aktas S, Okan SE. The effect on the optical absorption coefficients due to the positions in the plane of square $GaAs\ /\ Al(GaAs)$ quantum well wire under the laser field. Acta Physica Polonica. A 2019;136(6):882-888.
[20] You J, Guo K. Effect of terahertz laser field on anisotropic optical absorption and refractive index changes of coaxial square quantum well wires. Physica B: Physics of Condensed Matter 2021;615:413085.
[21] El-Yadri M, El Hamdaoui J, Aghoutane N, Pérez LM, Baskoutas S, Laroze D, Díaz P, El Feddi M. Optoelectronic Properties of a Cylindrical Core/Shell Nanowire: Effect of Quantum Confinement and Magnetic Field. Nanomaterials 2023;13(8):1334.
[22] Kavruk AE, Sahin M, Atav U. A detailed investigation of electronic and intersubband optical properties of $Al_xGa_{1-x}As/Al_{0.3}Ga_{0.7}As/Al_yGa_{1-y}As/Al_{0.3}Ga_{0.7}As$ multi-shell quantum dots. J. Phys. D: Appl. Phys. 2014;47:295302.
[23] Şahin M, Köksal K. The linear optical properties of a multi-shell spherical quantum dot of a parabolic confinement for cases with and without a hydrogenic impurity. Semiconductor Science and Technology 2012;27:125011.
[24] Kirak M, Yilmaz S. Third harmonic generation of spherical multilayered quantum dot: effects of quantum confinement, impurity, electric and magnetic fields. Applied Physics A 2022;128:459.
[25] Al EB, Kasapoglu E, Sakiroglu S, Sari H, Sökmen I, Duque CA. Binding energies and optical absorption of donor impurities in

spherical quantum dot under the applied magnetic field. Physica E-Low-Dimensional Systems& Nanostructures 2020;119:114011.
[26] Mathe L, Onyenegecha CP, Farcas AA, Pioraș-Țimbolmas LM, Solaimani M, Hassanabadi H. Linear and nonlinear optical properties in spherical quantum dots: Inversely quadratic Hellmann potential. Physics Letters A 2021;397:127262.
[27] Kaya D, Yücel MB, Bayrak MB. The total absorption coefficient and refractive index change of a spherical quantum dot in the confinement radial potential. Physica B: Condensed Matter 2023;648:414403.
[28] Aharoni A, Mokari T, Popov I, Banin U. Synthesis of $InAs/CdSe/ZnSe$ core/shell1/shell2 structures with bright and stable near-infrared fluorescence. Journal of the American Chemical Society 2006;128:257-264.
[29] Liu WH, Qu Y, Ban SL. Intersubband optical absorption between multi-energy levels of electrons in $InGaN/GaN$ spherical core-shell quantum dots. Superlattices and Microstructures 2017;102:373-381
[30] Rodríguez-Magdaleno KA, Perez-Alvarez R, Martínez-Orozco JC. Intra-mini band absorption coefficient in $GaAs/Al_xGa_{1-x}As$ core/shell spherical quantum dot. Journal of Alloys and Compounds 2018;736:211-215.
[31] Jafari AR. Optical properties of hydrogenic impurity in an inhomogeneous infinite spherical quantum dot. Physica B 2015;456:72–77.
[32] Al EB. Effect of the magnetic field, size, and donor position on the absorption coefficients related to a donor within the core/shell/shell quantum dot. Optical and Quantum Electronics 2021;53:676.
[33] Aktas S, Boz FK. The binding energy of hydrogenic impurity in a multilayered spherical quantum dot. Physica E-Low-Dimensional Systems &Nanostructures 2008;40(4):753-758.
[34] Aktas S, Boz FK, Bilekkaya A, Okan SE. The multilayered spherical quantum dot under a magnetic field. Applied Surface Science 2010;256(12):3832-3836.
[35] Zhang L, Li X, Zhao Z, Chang C, Duan Y. The influence of optical absorption under the external electric field and magnetic field of parabolic quantum dots. Indian Journal of Physics 2022;96(12):3645–3650.